



## Landmark detection in the chest and registration of lung surfaces with an application to nodule registration

Margrit Betke<sup>a,\*</sup>, Harrison Hong<sup>a</sup>, Deborah Thomas<sup>a</sup>, Chekema Prince<sup>a</sup>, Jane P. Ko<sup>b</sup>

<sup>a</sup>Computer Science Department, Boston University, Boston, MA 02215, USA

<sup>b</sup>Department of Radiology, New York University Medical School, New York, NY 10016, USA

Received 13 February 2002; received in revised form 24 November 2002; accepted 17 January 2003

### Abstract

We developed an automated system for registering computed tomography (CT) images of the chest temporally. Our system detects anatomical landmarks, in particular, the trachea, sternum and spine, using an attenuation-based template matching approach. It computes the optimal rigid-body transformation that aligns the corresponding landmarks in two CT scans of the same patient. This transformation then provides an initial registration of the lung surfaces segmented from the two scans. The initial surface alignment is refined step by step in an iterative closest-point (ICP) process. To establish the correspondence of lung surface points, Elias' nearest neighbor algorithm was adopted. Our method improves the processing time of the original ICP algorithm from  $O(kn \log n)$  to  $O(kn)$ , where  $k$  is the number of iterations and  $n$  the number of surface points. The surface transformation is applied to align nodules in the initial CT scan with nodules in the follow-up scan. For 56 out of 58 nodules in the initial CT scans of 10 patients, nodule correspondences in the follow-up scans are established correctly. Our methods can therefore potentially facilitate the radiologist's evaluation of pulmonary nodules on chest CT for interval growth.

© 2003 Elsevier Science B.V. All rights reserved.

**Keywords:** Computed tomography; Chest; Lung surfaces; Nodule registration

### 1. Introduction

Chest computed tomography (CT) has become a well-established means of diagnosing pulmonary metastases of oncology patients and evaluating response to treatment regimens. Since diagnosis and prognosis of cancer generally depend upon growth assessment, repeated CT studies are used to assess for growth of pulmonary nodules (Naidich, 1994; Yankelevitz et al., 2000).

Our long-term objective is to develop an image analysis system that assists the radiologist in detecting and comparing pulmonary nodules between two or more CT studies. Our main focus in this paper is nodule registration in metastatic disease. Other potential applications of our work

include functional lung imaging to evaluate asthma and emphysema and detection of primary lung cancer. Lung cancer remains the leading cause of cancer death in the United States, killing 160,000 people a year. The overall 5-year survival rate is only 15% (Landis et al., 1999), but early detection and resection of pulmonary nodules in Stage I can improve the prognosis to 67% (Mountain, 1997). The curability of early stage lung cancer has motivated researchers to propose CT-based lung-cancer screening (Henschke et al., 2002) and diagnostic image analysis systems (Reeves and Kostis, 2000).

Automated lung and nodule registration in CT has been addressed previously by our group (Betke et al., 2001, 2001; Betke and Ko, 1999; Ko et al., 2001), as well as by Brown et al. (2001), Kubo et al. (2001) and Shen et al. (2002). Our first system automatically segments the lungs and detects nodules in axial chest CT images, but human intervention was needed to match up the studies (Betke

\*Corresponding author.

E-mail addresses: [betke@cs.bu.edu](mailto:betke@cs.bu.edu) (M. Betke), <http://www.cs.bu.edu/faculty/betke> (M. Betke).

and Ko, 1999; Ko et al., 2001). In the current paper, we focus on automating the registration task. We describe a nodule registration method that is based on the three-dimensional (3D) alignment of anatomical landmarks and lung surfaces. We developed an attenuation-based feature matching approach that detects the trachea, vertebra and sternum and use the point-to-point registration method by Horn (1987) to align them with an optimal rigid-body transformation. This transformation is then applied to start an iterative process to align the lung surfaces.

A large body of literature has been published on registration techniques; see, for example, the surveys by Duncan and Ayache (2000), Audette et al. (2000) and Maintz and Viergever (1998). The focus has primarily been on developing and applying registration methods to brain images (e.g. Ferrant et al., 2001; Grimson et al., 1996; Maes et al., 1997; Maurer et al., 1996, 1998; Pelizzari et al., 1989; Roche et al., 2001; Viola and Wells, 1997). For the chest, radiographs (Kano et al., 1994) and MR images (Leleiveldt et al., 1999) have been matched temporally and CT studies have been registered to PET studies (Yu et al., 1995). CT-derived virtual bronchoscopic images have been matched to endoscopic views (Bricault et al., 1998). Registration of thoracic CT studies is challenging due to differences in inspiratory volumes between two studies. The patient's thorax is imaged while the patient is supposed to be in maximal inspiration. Not all patients, however, start out with and maintain maximal inspiration throughout the entire scan. In addition, the patient's torso may be rotated and translated differently each time a study is taken.

For detection and registration of nodules in chest CT, Brown et al. (2001) developed a rule-based system based on fuzzy logic that creates patient-specific models. Of 27 nodules in 17 patients, 22 nodules (81%) were relocated. To find the corresponding images in repeated CT scans, Kubo et al. (2001) developed a slice-by-slice method that uses landmarks and lung shape in the upper lung and vessels in the lower lung. Of 3502 CT slices of 60 patients, 3227 (92%) were correctly matched. Shen et al. (2002) describe a two-step method to align the CT scans first globally and then locally, and report an average nodule mismatch error of only a couple of millimeters. In our experiments, nodule correspondences for 56 (97%) out of 58 nodules of 10 patients are established correctly.

Our approach to chest registration is a combination of 3D landmark-, surface- and attenuation-based techniques. Similar techniques have been explored to register feature points and surfaces (Besl and McKay, 1992; Borgfors, 1988; Chui and Rangarajan, 2002; Chi and Rangarajan, 2001; Feldmar and Ayache, 1996; Ferrant et al., 2001; Guéziec et al., 2000; Johnson and Christensen, 2002; Pelizzari et al., 1989; Rangarajan et al., 1999; Sharp et al., 2002; Thirion, 1996), or match intensities of subimages (Althof et al., 1997; Kano et al., 1994; Weaver et al., 1998) or volumes (Maes et al., 1997; Rueckert et al., 1999; Viola and Wells, 1997). Various nonlinear optimization algo-

rithms are used to find the best alignments according to specific match measures (for a comparison of match measures, see (Holden et al., 2000; Rueckert et al., 1999)). We use three match measures—the Euclidean and the chamfer (Barrow et al., 1977) distances between corresponding surface points and the correlation between entire CT volumes.

Our algorithm improves the iterative closest-point (ICP) algorithm proposed by Besl and McKay (1992), Champleboux et al. (1992) and Zhang (1994) by including an efficient technique for determining correspondences of surface points. For other variants of the ICP algorithm, see (Eggert et al., 1998; Rusinkiewicz and Levoy, 2001). An exhaustive search for corresponding point pairs requires  $O(n^2)$  comparisons, where  $n$  is the number of points on the surfaces. Registration algorithms with  $O(n \log n)$  comparisons use octree (Champléoux et al., 1992) or  $k$ - $d$ -tree data structures (Feldmar and Ayache, 1996; Maurer et al., 1996). We apply Elias' algorithm (Rivest, 1974) to search for corresponding points in regions of increasing distance from the test point. Following the analysis by Rivest (1974) and Cleary (1979), we can show that the expected costs of establishing point correspondences are  $O(n)$ .

We do not use external fiducial points, such as skin-surface or bone-implanted markers (Malison et al., 1993; Maurer et al., 1998) which would be impractical in the clinical setting, and rely on patient-generated image content only. We do not require any manual input to compensate for large initial differences between CT studies, as is sometimes required by other methods (Pelizzari et al., 1989). We obtain a close alignment of the lung surfaces prior to applying the iterative algorithm by using the transformation that registers the anatomical landmarks optimally. Nonlinear optimization methods, such as the ICP method, generally work well on data with small initial misalignments (Besl and McKay, 1992; Maurer et al., 1996), even if they cannot guarantee convergence to the globally optimal solution.

## 2. Methods

Our system analyzes a pair of chest CT scans in three phases as illustrated in Fig. 1. In the first phase, anatomical landmarks are detected and registered in a point-to-point registration scheme (Sections 2.1 and 2.2). In the second phase, the points on the lung surface are collectively registered in a surface-to-surface registration scheme (Sections 2.3 and 2.4). In the last phase, the system finds correspondences between nodules located by a radiologist (Section 2.6).

### 2.1. Attenuation-based detection of anatomical landmarks

Two objectives guide the choice of landmarks. Firstly, to obtain reliable registration estimates, the landmarks

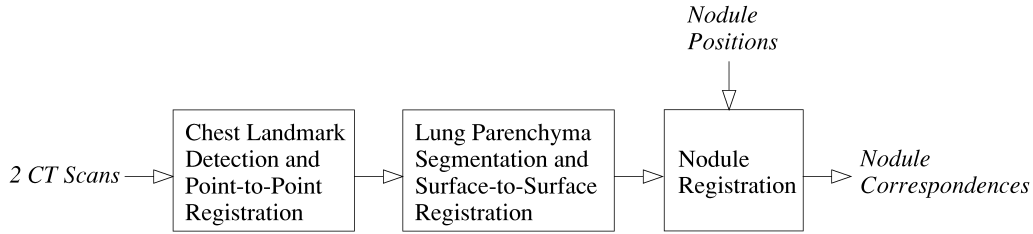


Fig. 1. System overview.

must be consistent despite variations in patient positions during the scans as well as changes in the chest due to disease progression and varying inspiratory volumes. Secondly, the landmarks must be chosen so that their positions and correspondences can be estimated both reliably and efficiently.

We chose the sternum and vertebra as landmarks, since they are bones with relatively fixed positions within the chest and have attenuation values ( $>600$  Hounsfield units (HU)) that are significantly different from those of the surrounding soft tissue (30–40 HU). The centers of the landmarks in the  $x \times y$  plane are used as estimates of landmark position; for example, the center of the spinal canal is used as the position of the vertebra. We also use the trachea as an anatomical landmark. Since it is an air-containing structure, its attenuation values are below  $-900$  HU. Although the trachea is not a rigid body, its position is relatively fixed within the chest if the patient is in maximal inspiration.

To detect a landmark in a CT image  $I$ , we use a template-based method that correlates the attenuation values of template image  $q$  with the attenuation values in a subimage  $I_q$  of  $I$ . The three template images used in our experiments are shown in Fig. 2. The normalized correlation coefficient quantifies how well the landmark in subimage  $I_q(x, y)$  matches the template image  $q(x, y; \mathbf{a})$ , where  $\mathbf{a}$  describes the affine parameters position, scale and rotation of the template landmark. The normalized correlation coefficient is defined by

$$r(\mathbf{a}) = \frac{1}{\sigma_I(\mathbf{a})\sigma_q(\mathbf{a})} \left( A(\mathbf{a}) \sum_{(x,y) \in O} I_q(x, y)q(x, y; \mathbf{a}) - \bar{I}_q(\mathbf{a})\bar{q}(\mathbf{a}) \right) \quad (1)$$

The sum is computed over a region  $O$  that is the union of all pixels that contain the expected feature,  $A(\mathbf{a}) = |O|$  is the number of pixels in  $O$ ,  $\bar{I}_q(\mathbf{a}) = \sum I_q(x, y)$  and  $\bar{q}(\mathbf{a}) = \sum q(x, y; \mathbf{a})$  are the respective local image sample means, scaled by  $A(\mathbf{a})$ , and  $\sigma_I^2(\mathbf{a}) = A(\mathbf{a}) \sum I_q(x, y)^2 - (\sum I_q(x, y))^2$  and  $\sigma_q^2(\mathbf{a}) = A(\mathbf{a}) \sum q(x, y; \mathbf{a})^2 - (\sum q(x, y; \mathbf{a}))^2$  are the respective local sample variances.

A set of subimages of  $I$  are tested to find the position of the subimage that best matches the template. The templates were manually cropped from a training CT scan, which was not included in our test data set. Although the template landmarks look slightly different in the test data, template and test data generally match well. Position estimates are obtained with correlations of at least 0.8, which lie far above the expected correlation  $E[r(\mathbf{a})] = 0$ . The normalized correlation coefficient serves as a match measure that is ‘information conserving’ because it exploits all the measured data relevant to the feature’s recognition. In our previous work (Betke and Makris, 2001), we showed when a statistically optimal estimator for the affine parameters takes the form of the normalized correlation coefficient.

The search for matching landmarks starts with the most cranial CT image and proceeds downward, slice by slice. Two tracheal landmarks are used for registration—the tracheal centroid in the most cranial image with visible lung (image A) and the tracheal centroid in the image at the carina (image B), where the trachea bifurcates into the right and left main stem bronchi, as shown in Fig. 2. To automatically identify images A and B, the attenuation CT images are converted into binary images using a threshold of  $-524$  Hounsfield units. This separates air-filled regions, such as lung and trachea, from denser areas. The connected components (Horn, 1986) within the binary images are then analyzed for position, shape and size (see Fig. 3). The

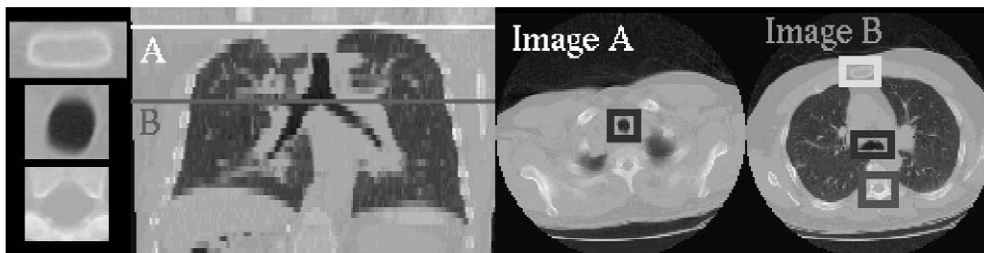


Fig. 2. On the left, generic template images of the sternum, trachea and vertebra. Next, a coronal view of a chest CT scan. The white line marks the most cranial image with visible lung (A), the gray line the axial image at the carina (B). On the right, axial views of images A and B with sternum (light gray), trachea (dark gray) and vertebra (medium gray).

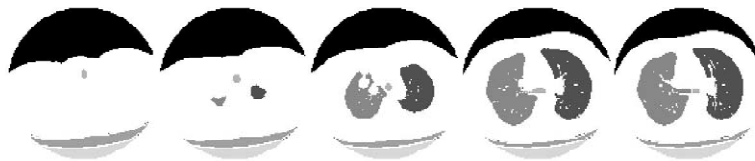


Fig. 3. The processed axial images 1, 4, 8, 15 and 16 of a low-resolution CT scan. The different connected components detected within an image are shown in differing shades of gray. Slice 1 shows the trachea as the only connected component within the chest. Slice 4 is the most cranial image with visible lung (image A). It contains a round trachea ( $e = 0.73$ ). Slice 15 is the image at the carina (image B). It contains a horizontally elongated trachea ( $e = 0.1$ ). The two connected components at the bottom of the carina in slice 16 demonstrate the separation of the tracheal airway into the bronchi.

topmost binary image generally only contains one component (see slice 1 in Fig. 3). Image A is detected when additional connected components appear (see slice 4 in Fig. 3). The shape of the trachea is measured by computing the ratio  $e = E_{\min}/E_{\max}$ , where  $E_{\min}$  and  $E_{\max}$  are the respective sums of the squared distances of tracheal points to the trachea's axes of least and most inertia (Horn, 1986). In images in which  $e$  is close to 1, the trachea is near circular (see slice 4 in Fig. 3). Once a considerable reduction of the ratio and an increase in size, followed by a dramatic decrease in size in the next slice, occurs, image B is detected. The generic sternum and vertebra templates, shown in Fig. 2, are used to find the sternum and vertebra in image B. For efficiency purposes, the respective search regions for the sternum and vertebra are restricted to the image portion anterior and posterior to the trachea.

The resolution of the correlation-based estimator can be improved by rotating and scaling the bone templates slightly, and by using 3D templates of landmarks, for example, the attenuation values in neighboring CT slices that comprise a full vertebra. Another option is to work with patient-specific templates that are manually cropped from scan 1 and then automatically detected in scan 2. In our experiments, however, generic 2D templates were sufficient, since the resolution of the correlation estimator is high.

## 2.2. Registration of two sets of corresponding points

Given the position  $\mathbf{x}$  of a chest landmark in an initial CT scan and the position  $\mathbf{p}$  in a follow-up scan, our goal is to find a 3D affine transformation  $\mathbf{p} = \mathbf{A}\mathbf{x} + \mathbf{x}_0$  that maps  $\mathbf{x}$  into  $\mathbf{p}$ , where vector  $\mathbf{x}_0$  describes translation and matrix  $\mathbf{A}$  rotation, scaling and skewing. In our application, the rotation parameters model the orientation of the patient's body on the CT table. We assume that the Cartesian coordinates of 3D points are preserved and CT reconstruction does not introduce skewing. The scaling parameters model the field of view ( $x$  and  $y$ ) and slice thickness ( $z$ ) differences between two CT scans. They are determined during CT image reconstruction, so we do not need to invert for them. Instead we adjust the two studies for scaling differences using the field-of-view and slice-thickness information included in the scan data. The problem then reduces to finding a rigid-body transformation

$$\mathbf{p} = \mathcal{T}(\mathbf{x}) = \mathbf{R}\mathbf{x} + \mathbf{x}_0, \quad (2)$$

where the matrix  $\mathbf{R}$  is orthonormal. Three point pairs are needed to solve this equation. Since there may be errors in the estimation of landmark positions, a greater accuracy in computing the transformation parameters may be obtained if more than three points are used.

To find the registration parameter that matches a set  $X$  of  $n$  points  $\mathbf{x}_1, \dots, \mathbf{x}_n$  in study 1 to a set  $P$  of corresponding points  $\mathbf{p}_1, \dots, \mathbf{p}_n$  in study 2, we minimize the sum of square residual errors

$$\sum_{i=1}^n \|\mathbf{p}_i - \mathcal{T}(\mathbf{x}_i)\|^2 = \sum_{i=1}^n \|\mathbf{p}_i - \mathbf{R}\mathbf{x}_i - \mathbf{x}_0\|^2, \quad (3)$$

with respect to the unknowns  $\mathbf{R}$  and  $\mathbf{x}_0$ . A closed-form optimal solution to this least-squares problem was given by Horn (1987) and is summarized in Appendix A. An advantage of Horn's solution is that the best possible transformation is computed in one step and an iterative scheme and initial guess are not required. An additional advantage is that the solution is symmetric, meaning that the solution that transforms  $X$  into  $P$  is the inverse of the solution that transforms  $P$  into  $X$ .

Horn's method is applied in the first phase of our registration method to compute the optimal rigid-body transformation of the four chest landmarks described in Section 2.1 (see Fig. 4).

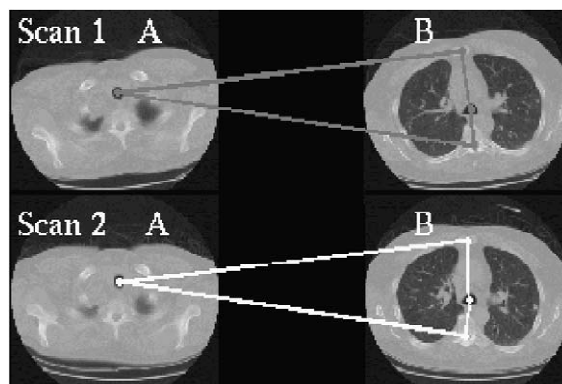


Fig. 4. Initial landmark registration. Four points used for registration are shown for each scan: the center of the trachea cross-section in slice A and the centers of the cross-sections of sternum, trachea and vertebra in slice B in each study. The landmarks in study 1 (gray) are then matched to the landmarks in study 2 (white).

### 2.3. Iterative surface registration

The point-to-point registration algorithm described above assumes that the correspondence between points in  $X$  and  $P$  has been established. For landmark points, correspondences can be established by correlation as described in Section 2.1, but the correspondences of surface point pairs are difficult to establish. For example, a lung border point in the right lung apex in scan 1 corresponds to *some* border point in the right apex in scan 2, but *which* physical point generally cannot be determined by a human observer. We therefore follow the standard ICP approach and define a correspondence mapping  $\mathcal{C}$  based on the distances between the points on the two surfaces. In particular, point  $\mathbf{x}_i$  in  $X$  is the corresponding point of  $\mathbf{p}_j$  in  $P$  if the Euclidean distance between  $\mathcal{T}(\mathbf{x}_i)$  and  $\mathbf{p}_j$  is the shortest among all distances between  $\mathbf{p}_j$  and any transformed point in  $X$ , i.e.,

$$\mathcal{C}(\mathbf{p}_j) = \mathbf{x}_i = \underset{\mathbf{x}_k \in X}{\operatorname{argmin}} \|\mathbf{p}_j - \mathcal{T}(\mathbf{x}_k)\|. \quad (4)$$

Eq. (4) applies to two point sets that may contain a different number of points. The correspondence mapping  $\mathcal{C}$  is many-to-one—several points on a surface in scan 1 may map to the same point on a surface in scan 2 and not all points in scan 2 may be assigned to some point in scan 1. In addition, there is an asymmetry: the mapping of points in  $P$  to points in  $X$  is generally different from the mapping of points in  $X$  to points in  $P$ . The corresponding point of  $\mathbf{x}_i$  is not necessarily  $\mathbf{p}_j$ , since the shortest distance among all distances between  $\mathcal{T}(\mathbf{x}_i)$  and any point in  $P$  may be shorter than  $\|\mathbf{p}_j - \mathcal{T}(\mathbf{x}_i)\|$ .

The paradoxical goals—to find corresponding points via registration and to register points via correspondence—are solved alternately. The flowchart of our lung surface registration algorithm is shown in Fig. 5. We first detect anatomical landmarks in studies 1 and 2 and compute the 3D affine transformation that registers them optimally. We then segment the lungs by converting the attenuation values in each CT slice into binary values and tracing the contour of each lung in each slice. We use a fixed threshold of  $-524$  HU to separate the lower attenuation air-filled lungs from the higher attenuation soft tissue structures and bone, as described by Ko et al. (2001). The segmented lung surfaces are then registered with the transformation parameters computed by the landmark registration. We establish correspondences based on the closest Euclidean distances between points, register the transformed lung borders in study 2 to the lung borders in study 1, determine the new point correspondences, compute the distance errors between corresponding points, and then iterate. Once the registration performance is sufficient, the process is terminated. The registration performance is considered sufficient when, from one iteration to the next, the change in the sum of squared distances (SSD), as defined in Eq. (3), becomes smaller than 1%.

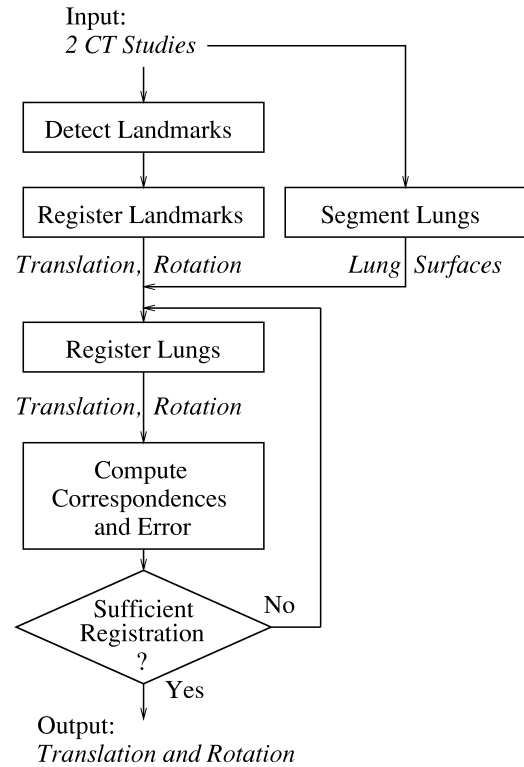


Fig. 5. Flowchart of the lung registration algorithm.

The lung registration algorithm converges monotonically to a local minimum of the least-squares registration error, as can be shown by adapting Besl's arguments (Besl and McKay, 1992). The choice of the initial registration parameters determines the rate of convergence and which local minimum is reached. Experimental results on the convergence performance are given in Section 4.

### 2.4. Neighborhood search for correspondences

A registration method must be computationally efficient so that it can eventually be employed in a clinical setting. For the ICP method, the computationally most extensive step is finding point correspondences. Tree data structures have been proposed (Champleboux et al., 1992; Feldmar and Ayache, 1996; Maurer et al., 1996) to reduce the number of required comparisons from  $O(n^2)$  for an exhaustive search to  $O(n \log n)$ . We designed a 'voxel space' data structure for Elias' algorithm (Rivest, 1974; Cleary, 1979). It decomposes the Euclidean 3D space into cubic neighborhoods and finds closest points by searching the neighborhoods in the order of increasing distance from the test point (see Fig. 6). The algorithm takes as input the points on surface  $P$  and the points on surface  $X$  that are transformed into the coordinate system of surface  $P$  for alignment.

#### 2.4.1. Cubic neighborhood search

For each point  $p$  on surface  $P$ :

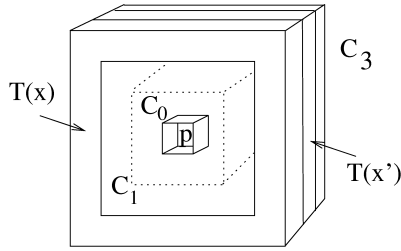


Fig. 6. The neighborhood search algorithm during the search for the transformed point in  $X$  that corresponds to  $\mathbf{p}$ . The voxel containing  $\mathbf{p} \in P$  is shown as cube  $C_0$ . Cubic neighborhood  $C_1$  is shown with dotted lines. Two points  $\mathcal{T}(\mathbf{x})$  and  $\mathcal{T}(\mathbf{x}')$  are found in cubic neighborhood  $C_3$ . Among the two, the point with the closest Euclidean distance to  $\mathbf{p}$  is the corresponding point.

1. Check if the voxels adjacent to  $p$  contain transformed points on surface  $X$ . Take advantage of the connectivity of  $P$  to avoid re-checking voxels.
2. If such points exist, select among them the point  $\mathcal{T}(\mathbf{x})$  with the smallest Euclidean distance to  $p$ . Otherwise expand the search space by one voxel in all directions.
3. Repeat step 2 until the closest transformed point  $\mathcal{T}(\mathbf{x})$  is found.

Note that the decomposition of the Euclidean space used here does not necessarily correspond to the voxel structure of the CT scans. The coordinates of the lung surface points in the CT scans are converted from voxel to millimeter units. This is convenient, because the mm-to-pixel ratios and slice thickness of the scans may differ. It is also convenient, because an arbitrarily coarse decomposition of the Euclidean space can be chosen. For example, a ‘voxel’ in our data structure can represent a  $1 \text{ mm}^3$  or  $5 \text{ mm}^3$  volume in 3D space.

We can adopt the average-case analysis of Elias’ algorithm by Rivest (1974) and Cleary (1979) to show that the expected costs of establishing  $n$  point correspondences are  $O(n)$ . In particular, for a given test point  $p$ , the number of voxels  $\beta$  examined by Elias’ algorithm is averaged over all data sets and test points. In this analysis,  $\beta$  does not depend on the number of surface points  $n$ , but instead on the density of the surface points. If the density is assumed

to be uniform,  $\beta$  is constant (Cleary, 1979). In our scenario, the points in  $P$  are not uniformly distributed throughout the scan, but instead clustered and collectively define a surface. This is more favorable for Elias’ algorithm, since the lung surfaces are never severely misaligned and the closest transformed point in  $X$  to test point  $p$  can be expected to be near  $p$ . In addition, the proximity of two neighboring surface points in  $X$  implies proximity of their corresponding points in  $P$  and an overlap of their cubic neighborhoods. As the alignment improves during the iterative process, the number of voxels  $\beta$  examined by the neighborhood search algorithm decreases.

### 2.5. Alternative alignment measures: chamfer distances and correlation

Surface registration algorithms based on the chamfer method use a preprocessed lookup table to determine the distance from a test point to a surface (Barrow et al., 1977). The lookup table contains a discrete distance map that decomposes the 3D space into voxels. This is similar to the decomposition of the 3D space into cubic neighborhoods as described above for our method. However, our data structure keeps track of points at a certain Euclidean distance, while the chamfer data structure only stores the distance to the closest surface point. Although the chamfer method does not establish point correspondences explicitly, it uses an error criterion similar to our method, namely the root mean square distance values, to evaluate an alignment. To evaluate an alignment of  $n$  surface points, both methods require  $O(n)$  computations.

Chamfer methods generally substitute the Euclidean metric with distance metrics similar to the city-block or  $L_1$  metric (Borgefors, 1988). We tested the two metrics shown in Fig. 7 to evaluate surface alignments. The first metric is a 3D version of a 2D metric proposed by Borgefors (1988) that takes into account the resolution differences in CT between pixel width and slice thickness. The version shown in Fig. 7 assumes a slice thickness of 5 mm and pixel width of 0.65 mm and must be adjusted for scans with other parameters. Our second metric is a Euclidean

#### Standard Chamfer Mask

Current slice:

4	3	4
3	0	3
4	3	4

Previous slice:

8	7	8
7	6	7
8	7	8

#### Euclidean Distance Mask

Current slice:

$\sqrt{2}w$	$w$	$\sqrt{2}w$
$w$	0	$w$
$\sqrt{2}w$	$w$	$\sqrt{2}w$

Previous slice:

$\sqrt{q^2 + 2w^2}$	$\sqrt{w^2 + q^2}$	$\sqrt{q^2 + 2w^2}$
$\sqrt{w^2 + q^2}$	$q$	$\sqrt{w^2 + q^2}$
$\sqrt{q^2 + 2w^2}$	$\sqrt{w^2 + q^2}$	$\sqrt{q^2 + 2w^2}$

Fig. 7. Image masks for preprocessing scan 2 with the chamfer method. The Euclidean distance mask accounts for slice thickness  $q$  and pixel width  $w$ .

metric that explicitly uses parameters for slice thickness  $q$  and pixel width  $w$ .

Since pixel widths generally differ between scan 1 and scan 2, scan 1 must first be transformed into the voxel lattice of scan 2 by resampling. When a rotation is applied to the resampled surface points of scan 1, the resulting voxel lattice generally does not match the lattice of scan 2 and therefore additional distance approximations must be made.

Alternatives to surface-based registration methods are ‘intensity-based registration methods’ (Althof et al., 1997; Kano et al., 1994; Maes et al., 1997; Rueckert et al., 1999; Viola and Wells, 1997; Weaver et al., 1998). We use the attenuation-based correlation measure defined in Eq. (1) to evaluate the alignment of the entire volumes of scan 1 and scan 2.

### 2.6. Nodule registration

To find nodule correspondences in repeated CT scans, the nodules of scan 1 are first transformed into scan 2 with the same rigid-body transformation that matches the lung surfaces optimally. The Euclidean distances are computed for all possible nodule pairings. Correspondences are then established by the pairs with the smallest distances. Fig. 8 shows the axial slices of two CT scans that contain corresponding nodules of large, increasing size.

### 2.7. Validation method

We apply the output transform of the surface registration algorithm to the structures within the lungs. The physical correspondences of these structures are easier to establish than those of lung surface points. We use two sets of points for validation—nodules and vessel branching points, which were marked manually. The rigid-body transformations that minimize the sums of the squared Euclidean distances between the nodule pairs and between the vessel pairs is computed (Eq. (3)). They serve as two ‘gold standard’ rigid-body transformations.

Note that the radiologist could misidentify corre-

sponding nodules or vessels. In addition, the location of the branching point or nodule centroid may be determined inaccurately and errors of a few pixel lengths in the  $x$  and  $y$  dimensions may occur. Errors in misidentifying the correct axial image have a more significant impact for studies with large slice thickness. To guarantee the accuracy of the vessel-based validation method, we take two precautionary measures: (1) the radiologist uses a large number of vessel branching points and (2) the points cover a large proportion of the lung volume. The reasoning is that the larger the number of points and the 3D space containing them, the smaller is the impact of potential measurement errors.

During the scanning, the patients were supposed to be in maximal inspiration. Lung volumes in the initial and follow-up scans should therefore be similar for patients who were able to maintain maximal inspiration throughout both scans. To estimate the lung volume for a particular study, we first segment the lung borders in each axial image. For each axial slice, the pixels enclosed by the left and right lung contours are then marked by a ‘flood fill algorithm’ (Foley et al., 1996). The marked pixels are converted into voxels by incorporating the slice thickness information. The resulting number of voxels is used as an estimate for lung volume.

## 3. Patient data

Ten patients were selected from the patients with thoracic CT scans taken for clinical indications at our institutions between 1993 and 2001. The patients were randomly selected by searching radiology reports for the terms ‘cancer’ and ‘pulmonary nodules’. A patient was excluded if he or she did not undergo follow-up CT. The process was repeated until 20 studies, two per patient, were found. The set of patients contains six female and four male patients. The interval of time between initial and follow-up studies ranges from 1 to 6.5 months.

Fourteen chest CT scans had been performed helically on GE HiSpeed Advantage machines. The CTs were obtained from above the lung apices through the adrenal glands using a 1:1 pitch either with 5 mm collimation for the entire study or 10 mm collimation with 5 mm collimation through the hila. Six studies were taken on a multi-helical Siemens Somatom Volume Zoom CT using a 1 mm collimator for the entire study and were reconstructed in 1.25 mm increments using a high-frequency reconstruction algorithm. The images were acquired with a  $512 \times 512$  matrix and quantized using 16 bits per pixel. Pixel width in the axial images ranges from 0.5 mm to 0.8 mm with an average of 0.65 mm and was different between scan 1 and scan 2 for patients 2–10. A thoracic radiologist determined the position of vessel branch points. An average of 35 vessel branch points and 5.8 nodules were used per case.

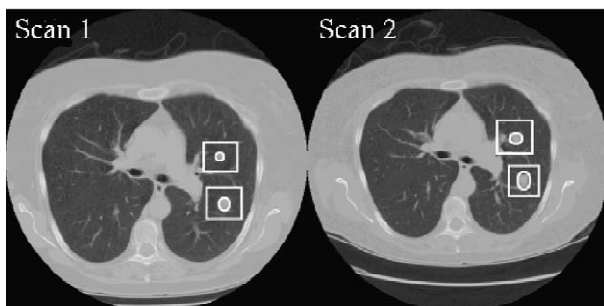


Fig. 8. Positions of two nodules in an initial and a follow-up scan.

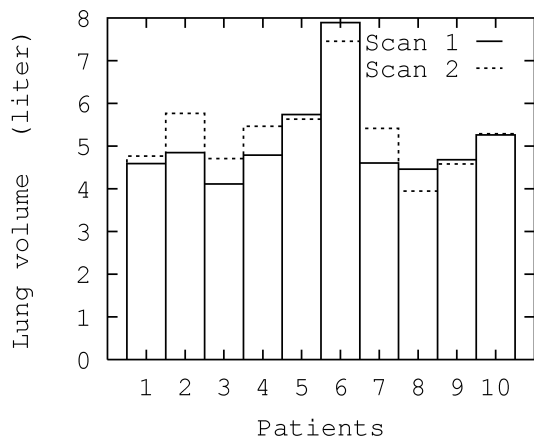


Fig. 9. Lung volumes for the initial and follow-up scans of 10 patients. Patients 2, 3, 4, 7 and 8 have large changes in volume (13.5%); the other five patients have small changes (2.8%).

#### 4. Results

Our landmark detection method succeeded in finding all 80 landmarks with good accuracy (within 5 pixels). The processing time to detect the tracheal landmarks depends on the number of slices in the data set above the carina. It takes 1.5 s on average to process each slice. Once image B is detected, it takes an average of 15 s to find the sternum and vertebra landmarks in image B.

The lung volumes of the 20 scans are shown in Fig. 9. The change in volume is 8.1% on average. There are five patients with a proportionately large change (13.5% on average), which indicates significant differences in inspiration between scans. Patient 7 was breathing significantly during the scanning. For the other five patients, a change of only 2.8% was measured on average.

The lung registration results are reported in Table 1 on a

per-point basis using the root mean squared error (RMS) between corresponding surface points and on a per scan basis using the sum of squared distances (SSD), as defined in Eq. (3). The average RMS error for rigid-body vessel alignment is also reported. The landmark registration (LR) algorithm reduces the initial SSD by 71% on average. If, as an alternative method to landmark registration, the surfaces in scan 1 are aligned along the principal axes of the surfaces in scan 2, the original SSD is reduced by only 46% on average. The most significant reduction of the initial misalignment (81%) is obtained with the landmark alignment and subsequent iterative surface registration algorithm (LSR). It has a better performance than the iterative surface registration without initial landmark alignment (SR). Fig. 10 shows the alignment of a lung before and after the LR and LSR algorithms are performed, Fig. 11 gives a zoomed-in view of an alignment, and Fig. 12 shows the proportional decrease of the SSD per ICP iteration.

The average running time of the LSR algorithm on an 866 MHz Pentium III processor is 9 min; 8 min for low-resolution (patients 1–7) and 12 min for high-resolution (patients 8–10) data (see in Table 2). Computationally, the most expensive step is establishing correspondences at each ICP iteration. The processing time per iteration decreases with the improvement of the alignment of the lung surfaces (see Fig. 13). Due to a better initial alignment, the LSR algorithm is significantly faster than the SR algorithm (see Fig. 14).

The average Euclidean distances between corresponding nodules before and after alignment are shown in Table 3. Nodule alignment based on the LSR algorithm has an average error of 8.0 mm. Figs. 15 and 16 visualize nodule and vessel registration results, respectively. Table 4 compares the nodule alignment based on the LSR algorithm to nodule alignment based on transformations that locally

Table 1  
Surface registration results

Patient No.	Gender	Time between studies (months)	Reconstruction interval (mm)	Lung volume difference	Surface RMS error (mm)			SSD error reduction		Iterations needed
					Vessel	SR	LSR	LR	LSR	
1	M	2	10/5/10	3.7%	8.9	6.2	5.4	61%	69%	5
2	F	4.5	10/5/10	15.9%	9.0	4.7	3.6	92%	94%	6
3	M	1.5	5	12.6%	4.8	4.4	4.1	77%	91%	11
4	F	2	5	12.3%	9.7	9.8	9.4	91%	93%	3
5	M	1.25	5	2.0%	15.6	14.5	4.3	97%	97%	3
6	F	1	5	5.9%	9.6	3.8	4.1	38%	83%	11
7	M	1.5	5	15.1%	9.7	5.3	4.5	53%	66%	11
8	F	4	1.25	12.9%	6.9	4.4	4.3	56%	65%	7
9	F	7	1.25	2.2%	7.3	1.8	1.8	22%	40%	8
10	F	6.5	1.25	0.5%	12.4	2.2	2.2	89%	97%	14
Average		3	–	8.1%	9.4	5.0	3.7	71%	81%	8

SSD: sum of squared Euclidean distances between corresponding surface points; RMS error, root mean squared Euclidean distances between corresponding surface points; SR: iterative surface registration without initial landmark alignment (25 iterations); LR: surface alignment based only on landmark registration; LSR: initial landmark and subsequent iterative surface registration.

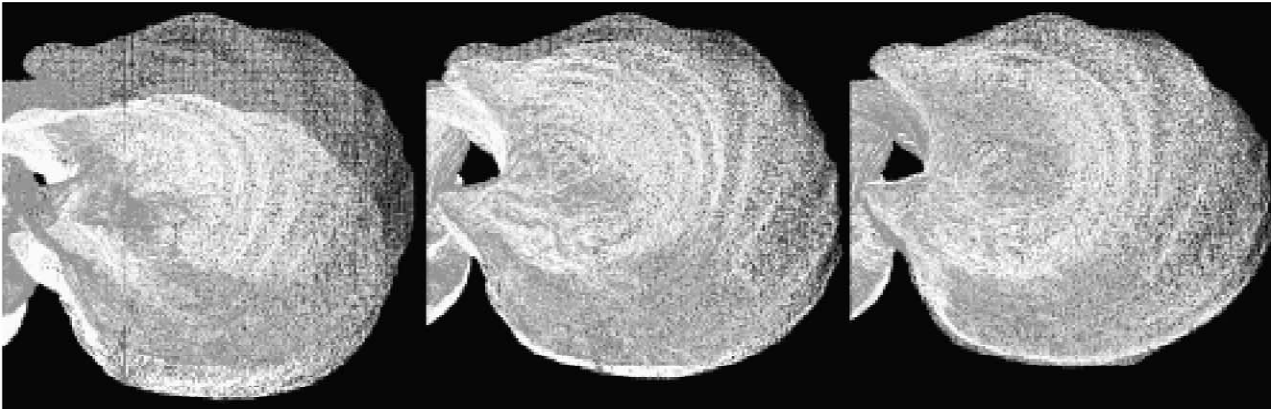


Fig. 10. Top views of the right lung of patient 8 are given before any processing (left), after the initial surface registration based on the landmark registration parameters (middle), and after 25 iterations of the lung surface registration (right). The surface in scan 1 is shown in gray; the surface in scan 2 in white.



Fig. 11. Registration results for high-resolution lung surfaces. The lung surfaces are shown on the top before (left) and after (right) registration. Zoomed-in views of the lungs are given below. The lungs in scan 1 are shown in gray and in scan 2 in white. The registration process shifted the surfaces in scan 2 to the left and slightly rotated them to align with the surfaces in scan 1.

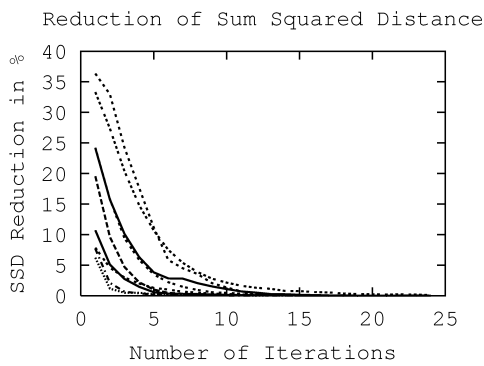


Fig. 12. Proportional reduction of the SSD per iteration of the registration algorithm for 10 CT pairs.

Table 2  
Average processing times

Procedure	Time (min)	
	Low Resolution data	High
Landmark detection and registration	1:25	5
Initial correspondences	1:39	
Average ICP iteration	0:44	
Iterative surface registration	6:45	
Overall algorithm	8	12
25 iterations of LSR	18	
25 iterations of SR	71	
Exhaustive search algorithm	52	1820

optimize the chamfer and correlation measures. The local optima were determined by an exhaustive six-dimensional search in the neighborhood of the best LSR solution. The local optima in the 6D search are at or near the LSR solution. SSD, chamfer and correlation values in the 2D subspace of translations in the axial plane are shown in Figs. 17 and 18. The chamfer values in Table 4 use the

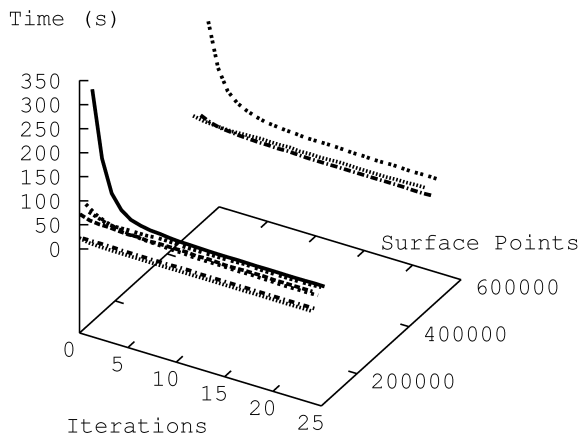


Fig. 13. Processing times of the neighborhood search algorithm decrease with each iteration of the lung registration algorithm for all 10 data sets. The first iteration takes up to a few minutes for data sets with large initial misalignment (e.g. solid curve for low-resolution data). Each iteration takes 43 s on average: 40 s for low-resolution data and 51 s for high-resolution data.

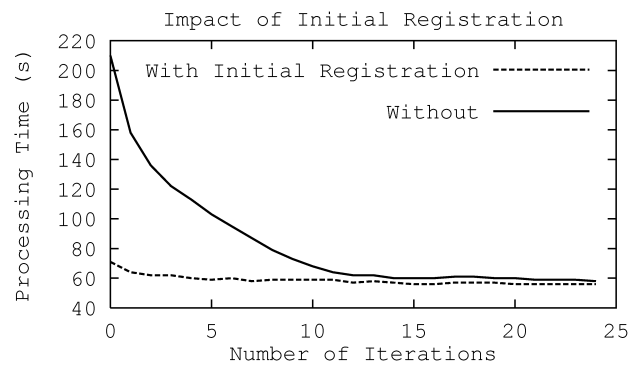


Fig. 14. The impact of initial landmark-based registration on the processing time of surface registration. Without initial registration, the first few iterations of the lung surface registration algorithm take several minutes for low resolution data (solid line). With initial registration, the processing time of the first iteration is reduced to a third and then drops below 1 min per iteration (dashed line).

Euclidean metric proposed in Section 2.5. The results for the other chamfer metric, designed for the 5 mm CT scans, are similar. Nodule correspondences for 56 (97%) out of 58 nodules of 10 patients are established correctly.

## 5. Discussion

### 5.1. Landmark detection

The landmarks in our data set have relatively similar appearances on CT. Their appearance may change due to metastatic disease in sternum or vertebrae and lung collapse. Lung collapse would result in a mostly horizontal shift of the location of the trachea. This would not cause difficulties for our algorithm since it searches for low attenuation regions to find the trachea in a slice above the lung apex. Connectivity is used to reduce the search space

Table 3  
Nodule registration results

Patient	Number of nodules	Average error (mm)		
		Without alignment	Alignment based on	
			Radiologist	LSR
1	15	35.6	7.1	17.0
2	7	24.7	2.8	3.3
3	7	18.3	5.5	8.5
4	4	32.6	1.8	4.2
5	4	56.9	2.5	5.1
6	3	29.7	1.7	5.9
7	2	17.0	–	10.6
8	4	11.4	3.1	5.5
9	4	15.8	1.6	15.6
10	8	26.6	3.3	4.7
Average	5.8	25.3	3.3	8.0

Average Euclidean distances between corresponding nodules before and after alignment based on nodule centroids and lung surfaces.

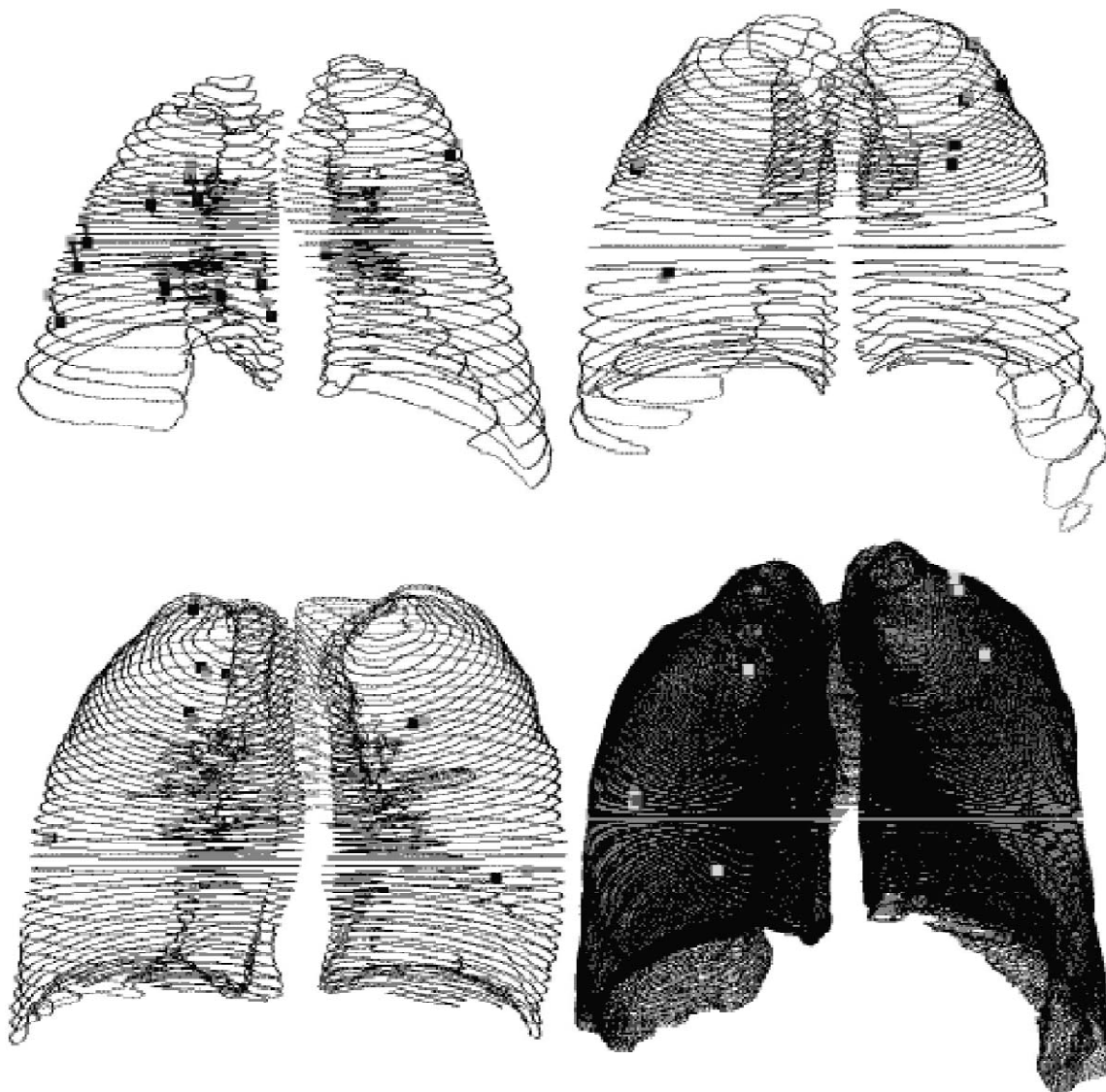


Fig. 15. Coronal views of lung surface contours in scan 2 for patients 1, 2, 3 and 10 with nodules in scan 2 (light grey) and nodules transformed from scan 1 into scan 2 (dark grey).

in lower slices and would help find the trachea even if it was shifted due to a lung collapse. Lung collapse is less common with metastatic disease, the focus of this paper, and more common with lung cancer. If a lung collapsed before scan 1 is taken, landmark detection and surface registration in the other lung will not be affected. If a lung collapsed between scan 1 and scan 2, a rigid-body transformation, however, will fail to provide an accurate model of the anatomical changes. This scenario may occur for lung cancer patients. Note, however, that our system is designed to work in conjunction with a radiologist who would be able to identify such a problem easily.

Metastatic disease in the sternum and the vertebrae expands the bone. The likelihood of involving every vertebral body and every portion of the sternum, however, is very low. The algorithm could be expanded, so that neighboring slices are tested, in the unlikely case that

sternum or vertebra were not found in image B, i.e. maximal correlation values were too small. If the lesion is asymmetric, the estimate of the landmark position may be shifted slightly. Such a small error in landmark detection will not affect the surface registration process significantly.

### 5.2. Landmark registration

Three non-collinear feature points are sufficient to invert Eq. (2). Due to the body's anatomy, three out of the four landmarks used can never be collinear. The three landmarks in image B, however, may be collinear. This means that the landmarks do not span the full 3D space of the chest, in particular, along the  $x$ -dimension. Small errors in estimating the  $x$ -coordinates of landmark positions therefore have a larger impact on the overall registration error than small errors in estimating the  $y$ - and  $z$ -coordinates. It

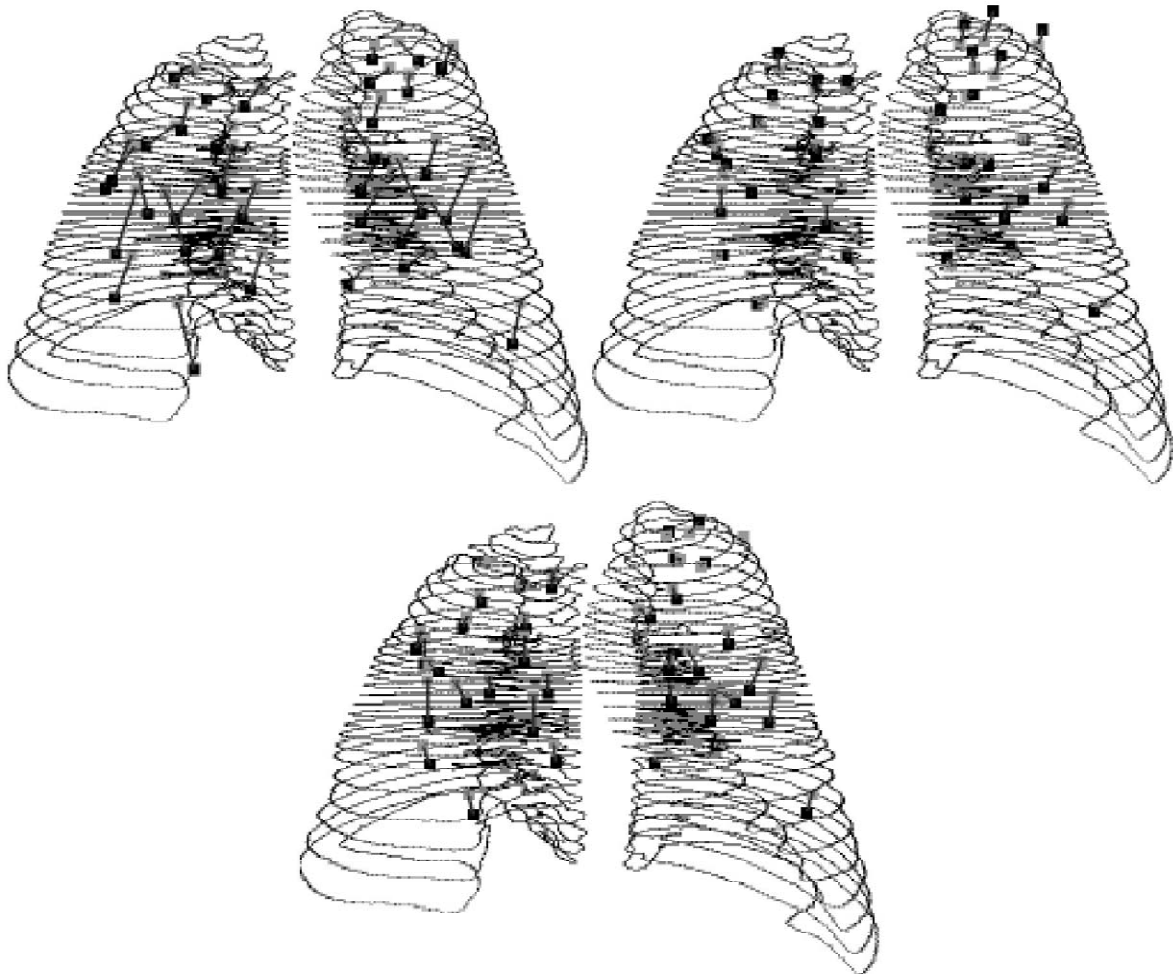


Fig. 16. Coronal views of the lung surface contours of study 2 for patient 1. On top, vessel points in study 1 (gray) and study 2 (black) are shown before registration. In the middle, the points in study 1 are aligned to the points in study 2 by the transformation that minimizes the SSD between the 36 vessel point pairs. On the bottom, the vessel points are matched using the transformation computed by the LSR algorithm.

follows that rotations in the sagittal ( $y \times z$ ) and coronal ( $x \times z$ ) planes can be estimated with more accuracy than rotations in the axial plane ( $x \times y$ ). To overcome this limitation, we would need to use lateral chest landmarks, for example, the ribs.

Correspondences between landmark pairs can be established easily; however, our detection method does not

guarantee that corresponding points are the same *physical* points. For example, if the patient is rotated counter-clockwise in the coronal plane (i.e. the left shoulder is closer to the head of the scanning table) in scan 1 but lies straight in scan 2, the most cranial image with visible lung may only contain the left lung in scan 1, but both lungs in scan 2. In this scenario, the trachea cross-section in image

Table 4  
Comparison of registration methods

Patient	Average error (mm)					Reduction of measures w.r.t. initial mismatch		
	Without alignment	Nodule alignment based on				Chamfer	Correlation	
		Radiologist	Vessels	LSR	Chamfer			Correlation
3	18.3	5.5	7.9	8.5	10.2	8.1	69%	36%
7	17.0	–	12.6	10.6	9.7	8.2	43%	9%
9	15.8	1.6	–	15.6	23.4	17.2	7%	5%
10	26.6	3.3	5.2	4.7	4.3	5.5	64%	54%
Average	25.3	3.3	8.5	9.9	11.9	9.8	46%	26%

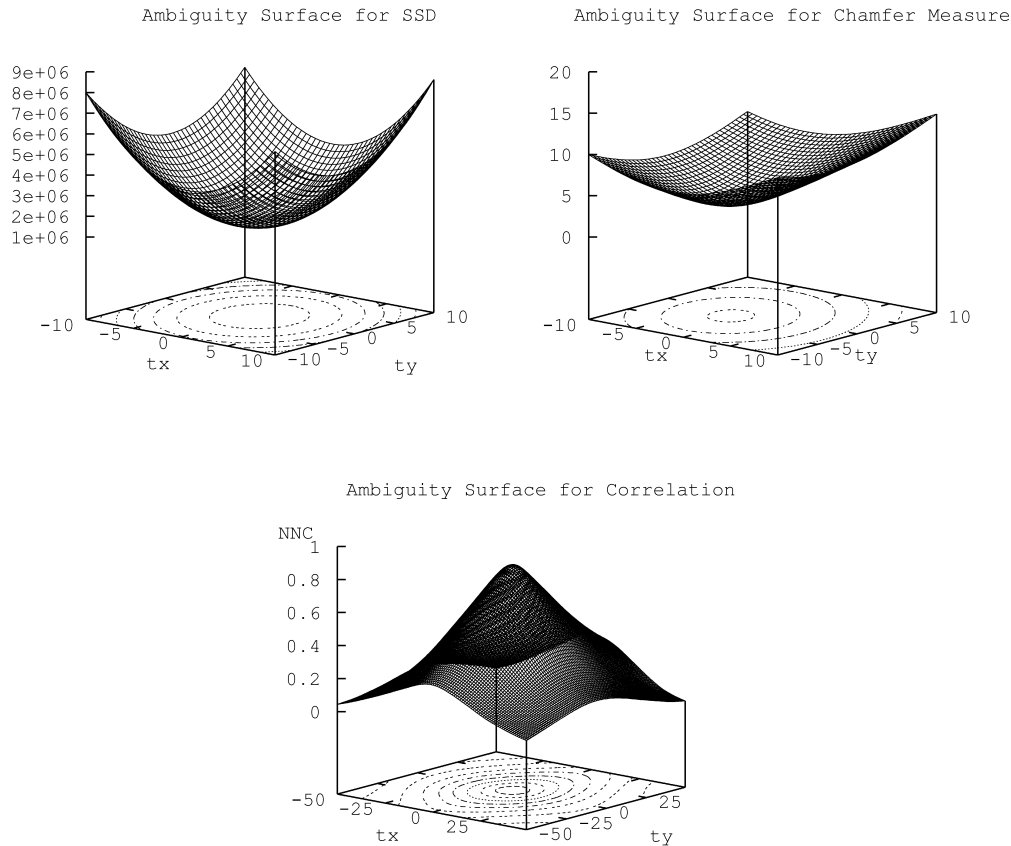


Fig. 17. Ambiguity surfaces for patient 3. Top left: the SSD in a local neighborhood defined by the LSR solution and translation offsets ( $t_x$ ,  $t_y$ ). Top right: the chamfer distances in the same neighborhood. The lowest average chamfer distance is 3.62, shown at  $(-1, 0)$ . The solution found by the LSR method is adjacent at  $(0, 0)$  and has an average chamfer distance of 3.64. Bottom: the values of the normalized correlation coefficient in a local neighborhood defined by the LSR solution. The peak of 0.87 of the ambiguity surface corresponds to the LSR solution.

A in scan 1 will be located above the trachea cross-section in image A in scan 2, and the cross-sections are therefore not images of the same part of the trachea. Note that such a scenario does not impact our overall registration performance, but only results in an initial misalignment that requires more processing time and surface registration

iterations to overcome. If a better initial landmark alignment is desired, 3D landmark templates should be used.

### 5.3. Lung surface registration

An iterative algorithm is called ‘stable’ or ‘robust’ if small variations in the starting point result in small differences in the output of the algorithm. Our method showed a stable performance in our experiments: two versions of our algorithm—surface registration with and without landmark alignment (LSR and SR)—converged to similar solutions. Their start points were relatively close due to prospective attention to patient positioning (see, for example, Fig. 10 left).

The accuracy of the lung surface registration depends on the accuracy of the lung segmentation. Small segmentation errors involving a few pixels on the boundary have a negligible effect on the registration, since the number of points on the surfaces range from several tens of thousands in the low-resolution scans to several hundred thousands in the high-resolution scans.

To reduce the processing time of our method, we can apply the iterative surface registration algorithm to a low-

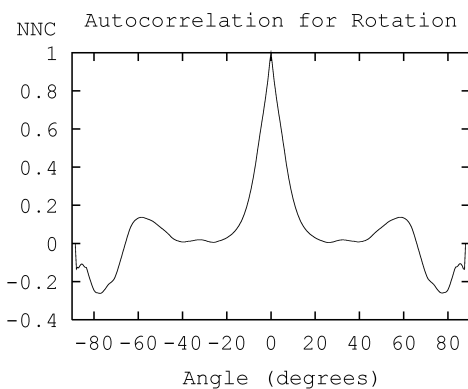


Fig. 18. The autocorrelation of an entire CT scan for  $\pm 90^\circ$  rotations around the  $z$ -axis. High correlations (above 0.8) are only found for a small range of rotation angles ( $\pm 2^\circ$ ).

resolution version of the surface data and then increase the resolution as needed. Our preliminary investigation (Hong et al., 2002) shows that this multilevel method is a useful alternative.

It is beyond the scope of this paper to develop and compare optimization techniques for chest registration based on the chamfer and correlation measures. A Gauss–Seidel algorithm, for example, could be adopted for the chamfer method (Borgefors, 1988) and simulated annealing could be used to search for the best correlation (Betke and Makris, 2001). It is instructive, however, to compare the ambiguity surfaces for the different methods. The shape of the peak of the surface characterizes the resolution of a method (Betke and Makris, 2001). The wider the peak, the smaller is the method’s resolution. In our experiments, the SSD measure has the highest resolution and the correlation measure the lowest among the three measures. Surface-based methods are often more efficient than volumetric methods. The running time of our algorithm and any chamfer method is  $O(kn)$  where  $n$  is the number of surface points and  $k$  the number of iterations. The running time of volumetric methods is generally  $O(kN)$  where  $N$  is the number of voxels evaluated.

#### 5.4. Nodule registration

The optimal rigid-body transformation of the nodules in our dataset resulted in an average misalignment of 3.3 mm. The transformation computed by the LSR method has an average misalignment that is more than twice as large and corresponds to an average distance of about 12 pixels in the axial images or six slices in the high-resolution scans. For our dataset, this produced a mismatch of only two nodules (3%). It could be argued that more mismatches will occur in data sets with many nodules located within a few pixels or slices of each other. However, the size of pulmonary nodules must also be taken into account. Small pulmonary nodules have diameters between 3 and 10 mm (Yankelevitz et al., 2000). They cover regions with diameters of 4–15 pixels. The resolution of our registration method therefore seems appropriate and our results should generalize to other data sets.

The resolution of the method also indicates that it could be used by a nodule detection system to relocate a nodule in scan 2 that was previously detected in scan 1. The detection system would need to focus only on a small region in scan 2 around the predicted nodule location. Our preliminary investigation of this topic is promising (Mullally et al., 2002).

The accuracy of the nodule registration results is not linked to differences in overall lung volume. In the case of the largest volume difference, one lung is about 1/6th larger than the other (patient 3). The seven nodules of this patient are rigidly aligned with an error smaller than the error for scan pairs with almost no volume difference, e.g. patients 1 and 10. This indicates that the small volume

differences for patient 1 and 10 are indeed due to locally large deformations, possibly near nodules, that result in small overall volume changes. Conversely, for data sets with large volume differences but accurate nodule registration, deformations may have occurred in regions that do not contain nodules.

Since the three match measures, i.e. the sum of squared Euclidean distances, average chamfer distances, and normalized correlation coefficient, attain local optima in the same small neighborhood in the space of solutions, they provide nodule alignments of similar accuracy (see Table 4). Note, however, that an optimal value for any of the measures does not necessarily describe a transformation that results in an optimal nodule alignment. For all three measures, we have found suboptimal surface alignments that result in more accurate nodule registration. The reason is that our rigid-body registration method can only approximate the true geometric relationship of the lungs.

## 6. Rigid versus non-rigid transformations

A higher degree of elasticity in the formulation of the registration transformation is needed to capture the true geometry of the lungs. This applies particularly to the apex and base of the lung, since lung deformations due to inspiration occur mainly in these regions (Napadow et al., 2001). Visual inspection of our results indicates that our registration method produces very good matches for most of the lung surface area, but that there are mismatches at the apex and base of the lungs for some of the scans. Similarly, when we apply the LSR algorithm to the vessel branching points, most mismatches are found in the periphery of the lung, in particular, the base of the lung (see Fig. 16). This also occurs when we apply the gold-standard rigid-body transformation to the vessels’ branching points.

We presented a *global* registration method—any change in a transformation parameter influences the transformation of the 3D data set as a whole (Audette et al., 2000). In a *local* transformation, such a change influences only a subset of the data. In future work, we plan to use local transformations to better capture the geometric relationships between surface portions at the lung apex as well as the lung base. For example, the ‘locally affine deformation algorithm’ proposed by Feldmar and Ayache (1996) may allow sufficient modeling of the deformations of lung apex and base and at the same time ensure that the global form of the lung is preserved.

A nonrigid alignment of the lung may also be guided by landmarks. The ribs are promising here, because they are at the periphery of the lung, move with respiration, and may be easily detected due to the high attenuation values of bones. Given a biomechanical model of respiratory changes of lung surfaces, ‘deformable surface models’ (Metaxas, 1997) may allow us to describe physical rather

than pure geometric transformations between lung surfaces.

Since our goal is to assist radiologists in detecting and comparing pulmonary nodules, we will need to model the shape and position of structures within the lungs, i.e. potential nodules, as functions of lung deformation during respiration, since these structures move with patient respiration. With such a model, accurate nonrigid alignment of lung surfaces may allow accurate alignment of the structures within the lung. Another route to explore is applying volumetric methods to the lungs only or to regions within the lungs, instead of the entire CT scans.

## 7. Summary and conclusions

We have developed a system for registering pulmonary CT scans. Our methods include chest landmark detection and alignment, iterative lung surface registration based on minimizing Euclidean distances of corresponding surface points, and nodule registration. We used manually established locations of pulmonary vessel branch points and nodules for validation. The correspondence of 56 out of 58 nodules in 10 pairs of CT scans was correctly identified. Our conclusions are as follows.

- A search process based on template matching can be used to detect anatomical landmarks in the chest reliably and efficiently. The measure of match is the normalized correlation coefficient applied to generic attenuation templates that comprise the landmarks.
- A close alignment of lung surfaces can be obtained by registering them with the same rigid-body transformation that matches the chest landmarks optimally.
- The landmark-based alignment of lung surfaces can be improved by re-registering them using a few iterations of a closest-point matching algorithm.
- The time needed to iteratively register the lung surfaces is significantly reduced by the initial landmark-based alignment.
- A cubic nearest neighbor search used in each iteration of the closest-point algorithm is an efficient linear-time method to establish surface point correspondences.
- A rigid-body transformation can provide a good approximation of the true geometric relationship of the lungs in maximal inspiration. Non-rigid transformations are needed to describe the alignment of lungs in differing respirational states.
- The use of three match measures, i.e. the sum of squared Euclidean distances, average chamfer distances, and normalized correlation coefficient resulted in nodule alignments of similar accuracy.
- Given the locations of nodules in two scans, nodule correspondences can be determined automatically. This may facilitate the radiologist's evaluation of changes in nodule size and shape and analysis of the patient's response to treatment regimens.

- The proposed registration method may also prove valuable in detecting nodule locations in follow-up scans and comparing structures or regions in the lung for functional analysis of asthma or emphysema patients.

In the future, we will integrate the proposed registration methods into our nodule detection system. We will also investigate techniques for non-rigid alignments of surfaces and volumes to find a method appropriate for the chest. Our long-term goal is to provide a system that becomes a clinically useful tool for nodule detection and growth assessment.

## Acknowledgements

The authors thank Shenghua Teng, Ph.D., Katelyn Mann, David Naidich, M.D., and Marilyn Noz, Ph.D., for their support. Financial support by the Whitaker Foundation, National Science Foundation, Office of Naval Research, and the Radiological Society of North America is also gratefully acknowledged.

## Appendix A. Inversion of a rigid-body transformation

This appendix summarizes Horn's method to compute the translation and rotation parameters of a rigid-body transformation that optimally aligns corresponding points in two datasets (Horn, 1987).

The best translation vector  $\mathbf{x}_0$  is  $\bar{\mathbf{x}} - \mathbf{R}\bar{\mathbf{p}}$ , the difference between the centroid  $\bar{\mathbf{x}} = 1/n \sum_{i=1}^n \mathbf{x}_i$  of point set  $X$  and the centroid  $\bar{\mathbf{p}} = 1/n \sum_{i=1}^n \mathbf{p}_i$  of point set  $P$  rotated by rotation  $\mathbf{R}$ . The translation can therefore be computed easily once the rotation is found. To find the rotation, the coordinates of points in  $X$  and  $P$  are converted into coordinates of points in  $X'$  and  $P'$  of coordinate systems that are originated at the respective centroids, e.g.  $\mathbf{x}'_i = \mathbf{x}_i - \bar{\mathbf{x}}$  for all  $\mathbf{x}_i \in X$ . This reduces the least-squares problem of Eq. (3) to a minimization of  $\sum_{i=1}^n \|\mathbf{x}'_i - \mathbf{R}\mathbf{p}'_i\|^2 = \sum_{i=1}^n \|\mathbf{x}'_i\|^2 - 2 \sum_{i=1}^n \mathbf{x}'_i{}^T \mathbf{R}\mathbf{p}'_i + \sum_{i=1}^n \|\mathbf{p}'_i\|^2$  with respect to rotation  $\mathbf{R}$  only, or  $\max_{\mathbf{R}} \sum_{i=1}^n \mathbf{x}'_i{}^T \mathbf{R}\mathbf{p}'_i$ . The rotation matrix

$$\mathbf{R} = \begin{bmatrix} q_0^2 + q_x^2 - q_y^2 - q_z^2 & 2(q_x q_y - q_0 q_z) & 2(q_x q_z - q_0 q_y) \\ 2(q_y q_x - q_0 q_z) & q_0^2 - q_x^2 + q_y^2 - q_z^2 & 2(q_y q_z - q_0 q_x) \\ 2(q_z q_x - q_0 q_y) & 2(q_z q_y + q_0 q_x) & q_0^2 - q_x^2 - q_y^2 + q_z^2 \end{bmatrix}, \quad (5)$$

solves this maximization problem, where  $q = (q_0, q_x, q_y, q_z)$  is the unit eigenvector that corresponds to the maximum eigenvalue of the symmetric matrix

$$N = \begin{bmatrix} s_{xx} + s_{yy} + s_{zz} & s_{yz} - s_{zy} & s_{zx} - s_{xz} & s_{xy} - s_{yx} \\ s_{yz} - s_{zy} & s_{xx} - s_{yy} - s_{zz} & s_{xy} + s_{yz} & s_{zx} + s_{xz} \\ s_{zx} - s_{xz} & s_{xy} + s_{yz} & -s_{xx} + s_{yy} - s_{zz} & s_{yz} + s_{zy} \\ s_{xy} - s_{yx} & s_{zx} + s_{xz} & s_{yz} + s_{zy} & -s_{xx} - s_{yy} + s_{zz} \end{bmatrix}, \quad (6)$$

and  $s_{kl}$  is the  $kl$ -th component of outer-product matrix  $S = \sum_i^n \mathbf{x}_i \mathbf{p}_i^T$ .

## References

- Althof, R.J., Wind, M.G.J., Dobbins, III J.T., 1997. A rapid and automatic image registration algorithm with subpixel accuracy. *IEEE Trans. Med. Imag.* 16 (3), 308–316.
- Audette, M.A., Ferrie, F.P., Peters, T.M., 2000. An algorithmic overview of surface registration techniques for medical imaging. *Medical Image Analysis* 4 (3), 201–217.
- Barrow, H.G., Tenenbaum, J.M., Bolles, R.C., Wolf, H.C., 1977. Parametric correspondence and chamfer matching: Two new techniques for image matching. In: *Proceedings 5th International Joint Conference on Artificial Intelligence*, Cambridge, MA, pp. 659–663.
- Besl, P.J., McKay, N.D., 1992. A method for registration of 3-D shapes. *IEEE Trans. Pattern Anal. Mach. Intell.* 14 (2), 239–256.
- Betke, M., Ko, J.P., 1999. Detection of pulmonary nodules on CT and volumetric assessment of change over time. In: Taylor, C., Colchester, A. (Eds.), *Medical Image Computing and Computer-Assisted Intervention—MICCAI'99*, Cambridge, UK. Springer-Verlag, Berlin, pp. 245–252.
- Betke, M., Makris, N.C., 2001. Recognition, resolution and complexity of objects subject to affine transformation. *Int. J. Comput. Vis.* 44 (1), 5–40.
- Betke, M., Hong, H., Ko, J.P., 2001a. Automatic 3D registration of lung surfaces in computed tomography scans. In: Niessen, W.J., Viergever, M.A. (Eds.), *Medical Image Computing and Computer-Assisted Intervention—MICCAI 2001: 4th International Conference*, Utrecht, The Netherlands. Springer-Verlag, Berlin, pp. 725–733.
- Betke, M., Hong, H., Ko, J.P., 2001b. Automatic 3D Registration of Lung Surfaces in Computed Tomography Scans, CS Technical Report 2001-004. Boston University.
- Borgefors, G., 1988. Hierarchical chamfer matching: a parametric edge matching algorithm. *IEEE Trans. Pattern Anal. Mach. Intell.* 10 (6), 849–865.
- Bricault, I., Ferretti, G., Cinquin, P., 1998. Registration of real and CT-derived virtual bronchoscopic images to assist transbronchial biopsy. *IEEE Trans. Med. Imag.* 17 (5), 703–714.
- Brown, M.S., McNitt-Gray, M.F., Goldin, J.G., Suh, J.W., Sayre, R.D., Aberle, D.R., 2001. Patient-specific models for lung nodule detection and surveillance in CT images. *IEEE Trans. Med. Imag.* 20 (12), 1205–1208.
- Champleboux, G., Lavallée, S., Szeliski, R., Brunie, L., 1992. From accurate range imaging sensor calibration to accurate model-based 3-D object localization. In: *Proceedings of the IEEE Computer Vision and Pattern Recognition Conference*, Champaign, IL. IEEE Computer Society, pp. 83–89.
- Chui, H., Rangarajan, A., 2000. A new algorithm for non-rigid point matching. In: *Proceedings of the IEEE Conference on Computer Vision and Pattern Recognition*, Vol. 2, pp. 44–51.
- Chui, H., Rangarajan, A., 2001. Learning an atlas from unlabeled point-sets. In: *Proceedings of the IEEE Workshop on Mathematical Methods in Biomedical Image Analysis*, Kawaii, Hawaii.
- Cleary, J.G., 1979. Analysis of an algorithm for finding nearest neighbors in Euclidean spaces. *ACM Trans. Math. Softw.* 5 (2), 183–192.
- Duncan, J.S., Ayache, N., 2000. Medical image analysis: progress over two decades and the challenges ahead. *IEEE Trans. Pattern Anal. Mach. Intell.* 22 (1), 85–105.
- Eggert, D.W., Fitzgibbon, A.W., Fisher, R.B., 1998. Simultaneous registration of multiple range views for use in reverse engineering of CAD models. *Image Vis. Comput.* 69 (3), 253–272.
- Feldmar, J., Ayache, N., 1996. Rigid, affine and locally affine registration of free-form surfaces. *Int. J. Comput. Vis.* 18 (2), 99–120.
- Ferrant, M., Nabavi, A., Macq, B., Jolesz, F.A., Kikinis, R., Warfield, S.K., 2001. Registration of 3-D interoperative MR images of the brain: Using a finite-element biomechanical model. *IEEE Trans. Med. Imag.* 20 (12), 1384–1397.
- Foley, J.D., van Dam, A., Feiner, S.K., Hughes, J.F., 1996. *Computer Graphics: Principles and Practice*. Addison-Wesley, MA.
- Grimson, W.E.L., Ettinger, G.J., White, S.J., Lozano-Pérez, T., Wells, III W.M., Kikinis, R., 1996. An automatic registration method for frameless stereotaxy, image guided surgery, and enhanced reality visualization. *IEEE Trans. Med. Imag.* 15 (2), 129–140.
- Guéziec, A., Wu, K., Kalvin, A., Williamson, B., Kanzanides, P., Van Vorhis, R., 2000. Providing visual information to validate 2-D to 3-D registration. *Medical Image Analysis* 4 (4), 357–374.
- Henschke, C.I., Yankelevitz, D.F., Libby, D., Kimmel, M., 2002. CT screening for lung cancer: the first ten years. *Cancer* 8 (Suppl 1:S), 47–54.
- Holden, M., Hill, D.L.G., Denton, E.R.E., Jarosz, J.M., Cox, T.C.S., Rohlfing, T., Goodey, J., Hawkes, D.J., 2000. Voxel similarity measures for 3-D serial MR brain image registration. *IEEE Trans. Med. Imag.* 19 (2), 94–102.
- Hong, H., Betke, M., Teng, S., Thomas, D., Ko, J.P., 2002. Multilevel 3D registration of lung surfaces in computed tomography scans—preliminary experience. In: *Proceedings of the International Conference on Diagnostic Imaging and Analysis*, Shanghai, China, pp. 90–95.
- Horn, B.K.P., 1986. *Robot Vision*. MIT Press, Cambridge, MA.
- Horn, B.K.P., 1987. Closed-form solution of absolute orientation using unit quaternions. *J. Opt. Soc. Am.* 4 (4), 629–642.
- Johnson, H.J., Christensen, G.E., 2002. Consistent landmark and intensity-based image registration. *IEEE Trans. Med. Imag.* 21 (5), 450–461.
- Kano, A., Doi, K., MacMahon, H., Hassell, D.D., Giger, M.L., 1994. Digital image subtraction of temporally sequential chest images for detection of interval change. *Med. Phys.* 21 (3), 453–461.
- Ko, J.P., Betke, M., Chest, C.T., 2001. Automated nodule detection and assessment of change over time—preliminary experience. *Radiology* 218 (1), 267–273.
- Kubo, M., Yamamoto, T., Kawata, Y., Niki, N., Eguchi, K., Ohmatsu, H., Kakinuma, R., Kaneko, M., Kusumoto, M., Moriyama, N., Mori, K., Nishiyama, H., 2001. CAD system for the assistance of comparative reading for lung cancer using serial helical CT images. In: Niessen, W.J., Viergever, M.A. (Eds.), *Medical Image Computing and Computer-Assisted Intervention—MICCAI 2001: 4th International Conference*, Utrecht, The Netherlands. Springer-Verlag, Berlin, pp. 1388–1390.
- Landis, S.H., Murray, T., Bolden, S., Wingo, P.A., 1999. Cancer statistics, 1999. *CA Cancer J. Clin.* 49 (1), 8–31.
- Leleiveldt, B.P.F., van der Geest, R.J., Ramze Rezaee, M., Bosch, J.G., Reiber, J.H.C., 1999. Anatomical model matching with fuzzy implicit surfaces for segmentation of thoracic volume scans. *IEEE Trans. Med. Imag.* 18 (3), 218–230.
- Maes, F., Collington, A., Vandermeulen, D., Marchal, G., Suetens, P., 1997. Multimodality image registration by mutual information. *IEEE Trans. Med. Imag.* 16 (2), 187–198.
- Maintz, J.B.A., Viergever, M.A., 1998. A survey of medical image registration. *Medical Image Analysis* 2 (1), 1–26.
- Malison, R.T., Miller, E.G., Greene, R., McCarthy, G., Charney, D.S., Innis, R.B., 1993. Computer-assisted coregistration of multislice SPECT and MR brain images by fixed external fiducials. *J. Comput. Assist. Tomogr.* 17 (6), 952–960.
- Maurer, C.R., Aboutanos, G.B., Dawant, B.M., Maciunas, R.J., Fitzpat-

- rick, J.M., 1996. Registration of 3-D images using weighted geometrical features. *IEEE Trans. Med. Imag.* 15 (6), 836–849.
- Maurer, C.R., Maciunas, R.J., Fitzpatrick, J.M., 1998. Registration of head CT images to physical space using a weighted combination of points and surfaces. *IEEE Trans. Med. Imag.* 17 (5), 753–761.
- Metaxas, D.N., 1997. *Physics-Based Deformable Models: Applications to Computer Vision, Graphics, and Medical Imaging*. Kluwer Academic Press, Boston.
- Mountain, C.F., 1997. Revisions in the international system for staging lung cancer. *Chest* 111 (6), 1710–1717.
- Mullally, W., Betke, M., Hong, H., Mann, K., Ko, J.P., 2002. Multi-criterion 3D segmentation and registration of pulmonary nodules on CT: a preliminary investigation. In: *Proceedings of the International Conference on Diagnostic Imaging and Analysis*, Shanghai, China, pp. 176–181.
- Naidich, D.P., 1994. Helical computer tomography of the thorax. *Radiol. Clin. North Am.* 32 (4), 759–774.
- Napadow, V.J., Mai, V., Bankier, A., Gilbert, R.J., Edelman, R., Chen, Q., 2001. Determination of regional pulmonary parenchymal strain during normal respiration using spin inversion tagged magnetization MRI. *J. Magn. Reson. Imag.* 13 (3), 467–474.
- Pelizzari, C.A., Chen, G.T., Spelbring, D.R., Weichselbaum, R.R., Chen, C.T., 1989. Accurate three-dimensional registration of CT, PET and/or MR images of the brain. *J. Comput. Assist. Tomogr.* 13, 20–26.
- Rangarajan, A., Chui, H., Duncan, J., 1999. Rigid point feature registration using mutual information. *Medical Image Analysis* 3 (4), 425–440.
- Reeves, A.P., Kostis, W.J., 2000. Computer-aided diagnosis for lung cancer. *Radiol. Clin. North Am.* 38 (3), 497–509.
- Rivest, R.L., 1974. On the optimality of Elias's algorithm for performing best-match searches. In: *Information Processing '74 (Proc. IFIP Conference)*, Stockholm. North Holland, pp. 678–681.
- Roche, A., Pennec, X., Malandain, G., Ayache, N., 2001. Rigid registration of 3-D ultrasound with MR images: a new approach combining intensity and gradient information. *IEEE Trans. Med. Imag.* 20 (10), 1038–1049.
- Rueckert, D., Sonoda, L.I., Hayes, C., Hill, D.L.G., Leach, M.O., Hawkes, D.J., 1999. Nonrigid registration using free-form deformations: application to breast MR images. *IEEE Trans. Med. Imag.* 18 (8), 712–721.
- Rusinkiewicz, S., Levoy, M., 2001. Efficient variants of the ICP algorithm. In: *Third IEEE International Conference on 3-D Digital Imaging and Modeling*, pp. 145–152.
- Sharp, G.C., Lee, S.W., Wehe, D.K., 2002. ICP registration using invariant features. *IEEE Trans. Pattern Anal. Mach. Intell.* 24 (1), 90–102.
- Shen, H., Fan, L., Qian, J., Odry, B.L., Novak, C.L., Naidich, D.P., 2002. Real-time and automatic matching of pulmonary nodules in follow-up multi-slice CT studies. In: *Proceedings of the International Conference on Diagnostic Imaging and Analysis*, Shanghai, China, pp. 101–106.
- Thirion, J.-P., 1996. New feature points based on geometric invariants for 3D image registration. *Int. J. Comput. Vis.* 18 (2), 121–137.
- Viola, P., Wells, W.M., 1997. Alignment by maximization of mutual information. *Int. J. Comput. Vis.* 24 (2), 137–154.
- Weaver, J.B., Healy, D.M., Periaswamy, S., Kostelec, P.J., 1998. Elastic image registration using correlations. *J. Digital Imag.* 11 (3, Suppl. 1), 59–65.
- Yankelevitz, D.F., Reeves, A.P., Kostis, W.J., Zhao, B., Henschke, C.I., 2000. Small pulmonary nodules: volumetrically determined growth rates based on CT evaluation. *Radiology* 217 (1), 251–256.
- Yu, J.N., Rahey, F.H., Gage, H.D., Eades, C.G., Harkness, B.A., Pelizzari, C.A., Keyes, Jr. J.W., 1995. Intermodality, retrospective image registration in the thorax. *J. Nucl. Med.* 36 (12), 2333–2338.
- Zhang, Z., 1994. Iterative point matching for registration of free-form curves and surfaces. *Int. J. Comput. Vis.* 13 (2), 119–152.